

# From foreshock to mainshock: transient sliding velocity sets nucleation time

**Barnaby Fryer**

`barnaby.fryer@geoazur.unice.fr`

Université Côte d'Azur, CNRS, Observatoire de la Côte d'Azur, IRD, Géoazur <https://orcid.org/0000-0002-4021-1238>

**Dmitry Garagash**

Department of Civil and Resource Engineering, Dalhousie University

**Mathias Lebihain**

Navier, ENPC, Univ Eiffel, CNRS UMR8205 <https://orcid.org/0000-0002-2233-4701>

**François Passelègue**

CNRS <https://orcid.org/0000-0002-4217-9817>



---

**Physical Sciences - Article**

**Keywords:**

**Posted Date:** October 13th, 2025

**DOI:** <https://doi.org/10.21203/rs.3.rs-7702556/v1>

**License:**   This work is licensed under a Creative Commons Attribution 4.0 International License.  
[Read Full License](#)

**Additional Declarations:** There is **NO** Competing Interest.

---

# From foreshock to mainshock: transient sliding velocity sets nucleation time

Barnaby Fryer<sup>1,\*</sup>, Dmitry Garagash<sup>2</sup>, Mathias Lebihain<sup>3</sup>, and François Passelègue<sup>1</sup>

<sup>1</sup>Université Côte d'Azur, CNRS, Observatoire de la Côte d'Azur, IRD, Géoazur, Sophia Antipolis, France.

<sup>2</sup>Department of Civil and Resource Engineering, Dalhousie University, Halifax, Canada.

<sup>3</sup>Navier, ENPC, Institut Polytechnique de Paris, Univ Gustave Eiffel, CNRS, Marne-la-Vallée, France.

\*barnaby.fryer@geoazur.unice.fr@cnrs.fr

## ABSTRACT

Coseismic rupture is commonly preceded by stable fault slip, which may accelerate into dynamic rupture as the slip front reaches critical velocities. However, the physical conditions that govern this nucleation process remain poorly constrained. Classical theoretical frameworks typically neglect perturbations such as foreshocks, yet these may critically influence rupture evolution. Here, we present laboratory experiments that generate dynamic rupture events exhibiting nucleation phases with durations spanning two orders of magnitude. When nucleation onset is associated with a foreshock, its size reliably constrains the transient sliding velocity between the foreshock and the ensuing mainshock. This transient velocity, in turn, governs both the size and duration of the nucleation phase in both experimental and natural earthquakes. Our results align with a theoretical framework based on a rate-dependent Griffith-like equation of motion, formulated using rate-and-state friction, and controlled by two key parameters: a characteristic impulse and overstress. Notably, we demonstrate that, depending on these governing parameters, a foreshock may alternatively lead to either arrested nucleation and no mainshock rupture, or merge directly into the mainshock. Moreover, this framework enables inversion for key fault friction parameters governing earthquake nucleation.

Understanding the nucleation of frictional ruptures is a central challenge in earthquake mechanics<sup>1</sup>. Beyond earthquake physics, nucleation processes are generic to frictional instabilities. Nucleation refers to the early processes that initiate fault rupture, marking the transition from a stable, locked fault to an unstable, dynamically slipping one. Coseismic rupture is theoretically expected to be preceded by quasi-static slip, growing in space and time until it reaches a critical size that may trigger dynamic failure<sup>1–7</sup>. This behavior is observed in both rate-and-state<sup>3,6,8,9</sup> and slip-weakening models<sup>2,4,5,10</sup>. These foundational studies suggest that the nucleation length, a critical measure of the size of the slipping zone prior to dynamic rupture, is primarily governed by the fracture energy of the fault interface,  $G_c$ , and the weakening rate within the nucleation region<sup>5</sup>. However, the physical parameters that control the duration and detectability of this stable phase remain poorly understood<sup>8,11</sup>. As a result, it is still unclear under which conditions geophysical observations might reveal precursory signals. Some earthquakes appear to be preceded by a prolonged nucleation stage<sup>12–17</sup>, potentially accompanied by foreshocks<sup>13–16,18,19</sup>, while many others exhibit no detectable dynamic precursor activity at all. These contrasting observations highlight the need for further investigation into the various physical mechanisms that may govern earthquake nucleation. Key open questions include (i) whether all earthquakes exhibit nucleation, (ii) how foreshocks affect nucleation, and (iii) whether the slip distance governing dynamic rupture also applies to nucleation.

We report laboratory experiments that, for the first time, directly capture how foreshocks control the nucleation of earthquakes. A small initial slip event sets the transient sliding velocity, which in turn dictates the duration and scale of the nucleation phase before dynamic rupture. Our results are supported by a theoretical framework based on a rate-dependent Griffith-like equation of motion, formulated using rate-and-state friction. Finally, we extend this theoretical framework to natural earthquakes preceded by foreshocks, enabling constraint of the characteristic nucleation parameters of large earthquakes, challenging standard estimates.

## Two decades of nucleation duration in similar stress states

Experiments were conducted using a biaxial loading apparatus (Fig. 1a; see Methods for details). Three representative nucleation phases from a single experiment are shown in Fig. 1b–e. Despite having nearly identical initial stress conditions (Figs. 1b), the duration of the nucleation phase varied by over an order of magnitude, ranging from 0.6 to 12.7 msec (Fig. 1e–g), and reached maximum values of  $\approx 80$  msec across the experimental suite, highlighting the intrinsic complexity of nucleation dynamics.

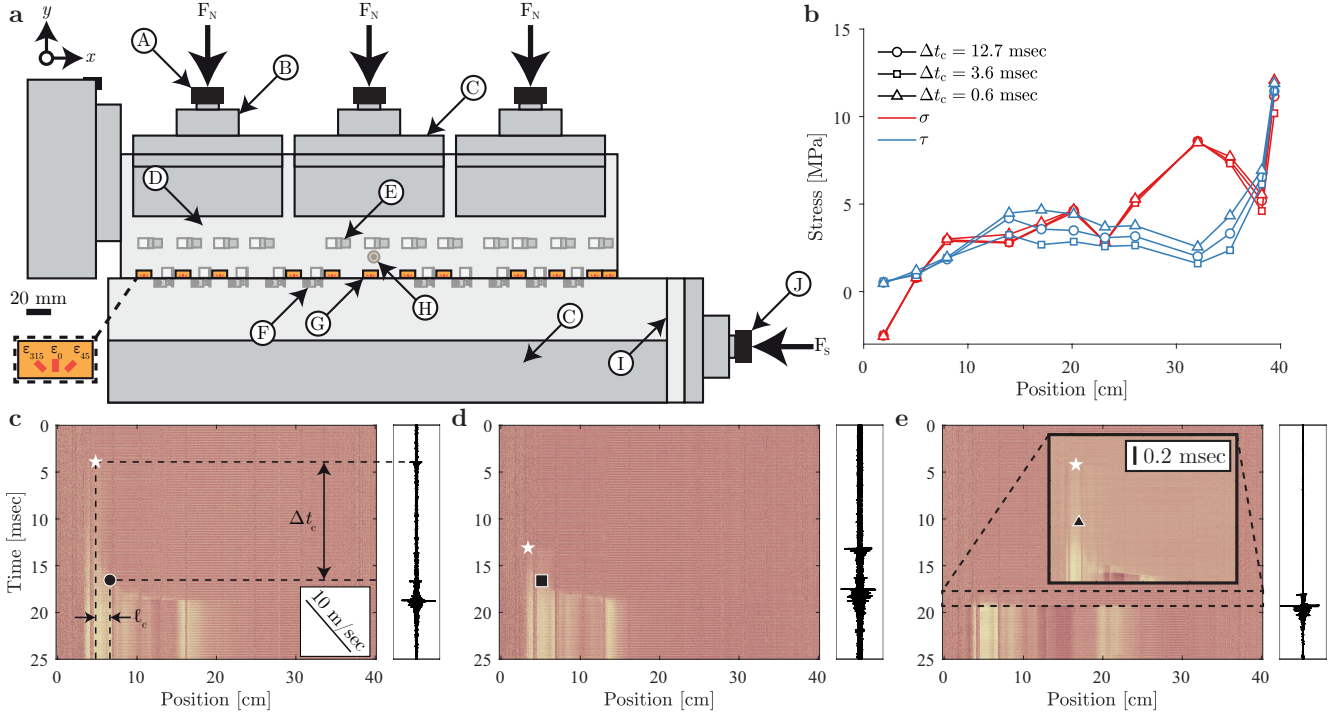


**Figure 1. Large variations in nucleation duration despite similar stress states.** **a**, The experimental setup of frictional stick-slip experiments. Two PMMA blocks (D) with lengths, widths, and heights of  $(x,y,z) = (40,10,1)$  cm and  $(x,y,z) = (45,10,1.8)$  cm are contained in a steel sample holder (C). A normal load is first applied by three vertical hydraulic pistons (A), with its nominal value given by an analogue gauge and value in force measured by a load cell (B). Then, a shear load is applied via a fourth piston (J) by a hydraulic pump at a constant injection rate. A spacer can be adjusted to allow for varied stress states (I). Twelve strain gauge rosettes are located at  $y = 3$  mm (G). Ten displacement sensors measure local slip (F). Twelve horizontally-oriented accelerometers are located at  $y = 30$  mm (E). One piezoelectric sensor is used to trigger a high-speed camera and synchronize all recording systems (H). The use of the high-speed camera with a polarized light source and the photoelastic properties of PMMA allows for the tracking of the propagating crack tip. **b-e**, Three example events which are the 6<sup>th</sup>, 2<sup>nd</sup>, and 9<sup>th</sup> dynamic events, respectively, recorded from the same experiment at a nominal normal stress of 150 bar but with different nucleation durations (12.7, 3.6, and 0.6 msec). **b**, The stress profiles 0.5 seconds prior to the dynamic events. **c-e**, The corresponding videograms of the dynamic events, allowing for a visualization of rupture progression. The acceleration recorded by the left-most accelerometer is shown to the right of the videogram. Nucleation is taken to begin with a foreshock recorded by the accelerometers (white star) and to be achieved when rupture velocity reaches 10 m/sec (black shape corresponding to specific event), allowing for the calculation of nucleation duration,  $\Delta t_c$ , and length,  $\ell_c$ . Nucleation duration is shown to vary by over an order of magnitude during one experiment at similar stress conditions during non-sequential events.

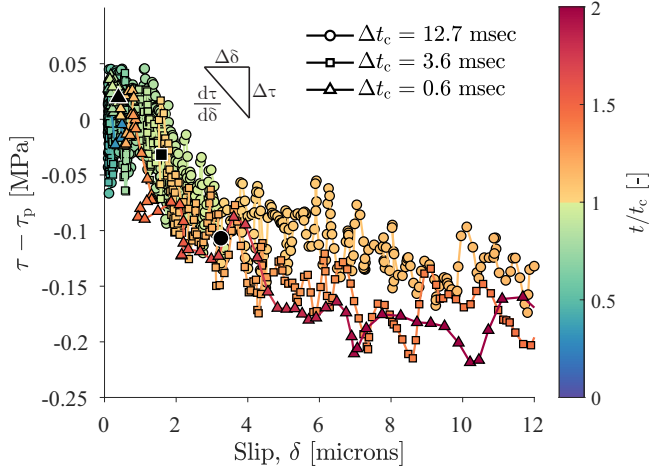


**Figure 2. Comparable weakening rates for an order of magnitude difference in nucleation duration.** The weakening (change of shear stress) as a function of slip within the nucleating patch. The figure corresponds to the same three events shown in Fig. (1). These three events occurred at similar normal (0.8, 0.8, and 0.9 MPa) and peak shear (1.1, 1.1, and 1.4 MPa) stresses. The color bar indicates the time normalized by the nucleation duration and a black shape corresponding to the event indicates the moment nucleation is considered to be achieved.

Note that the three selected representative nucleation phases are observed to initiate with a foreshock (Fig. 1c-e, S1g-i, S3a-c). In many cases, additional foreshocks can be clearly identified prior to the onset of the main rupture (Fig. S1g,h). The initiation of nucleation with a distinct foreshock is a consistent feature across the experimental dataset. The primary exceptions are events in which no discernible nucleation phase is present; in these instances, the initial foreshock evolves directly into dynamic rupture, without the intermediate stage of quasi-static slip-front propagation (Fig. S7).

## Weakening rate does not control nucleation duration

As slip,  $\delta$ , initiates within the nucleating patch, the shear stress,  $\tau$ , begins to decrease, reflecting fault weakening. Initially, the slip-weakening rate,  $\frac{d\tau}{d\delta}$ , is steep, meaning a substantial stress drop occurs over a small amount of slip. However, the weakening rate progressively decreases as slip continues, eventually approaching a quasi-steady residual shear stress level (Fig. 2). Previous studies have shown that sharper weakening rates result in smaller nucleation lengths<sup>4,5</sup>. These studies generally indicate that weakening rate has a similar effect on nucleation duration. Yet, the example events show similar weakening rates despite an order of magnitude difference in nucleation duration (Fig. 2). Moreover, the two orders of magnitude variation in nucleation durations observed across the full experimental suite cannot be easily attributed to differences in weakening rate. In fact, the initial weakening appears to be pressure insensitive, i.e., non frictional, as the drop in strength is essentially constant despite significant differences in normal stress for many events.

## Foreshocks and the onset of sliding

While the stress criticality does not appear to vary significantly between cases of slow and rapid nucleation (Fig. 1b), the initial impulse imparted to the nucleating patch does. The initial foreshock generates a burst of sliding velocity along the fault. This rapidly decays to a minimum transient sliding velocity,  $V_{\min}$ , (Fig. 3a,b). The value of  $V_{\min}$  is found to be positively correlated with the size of the foreshock, such that larger foreshocks produce higher transient sliding velocities (Fig. 3b,c). This relationship suggests that the initial energy imparted by the foreshock plays a key role in controlling the evolution and duration of the nucleation phase.

Effectively, a clear relationship emerges between nucleation duration and foreshock size (Fig. 4a): events with longer nucleation phases are typically preceded by smaller foreshocks and accumulate greater amounts of quasi-static slip prior to transitioning to dynamic rupture. This trend is not only evident in the present experimental dataset, but also appears consistent with observations from larger-scale laboratory experiments and natural earthquakes (Fig. 4a). A general pattern of nucleation behavior can thus be identified (Fig. 3a,b). The sequence begins with a foreshock that triggers a burst in sliding velocity locally along the fault. This sliding velocity then decays to a minimum, i.e. the so-called transient sliding velocity  $V_{\min}$ , corresponding

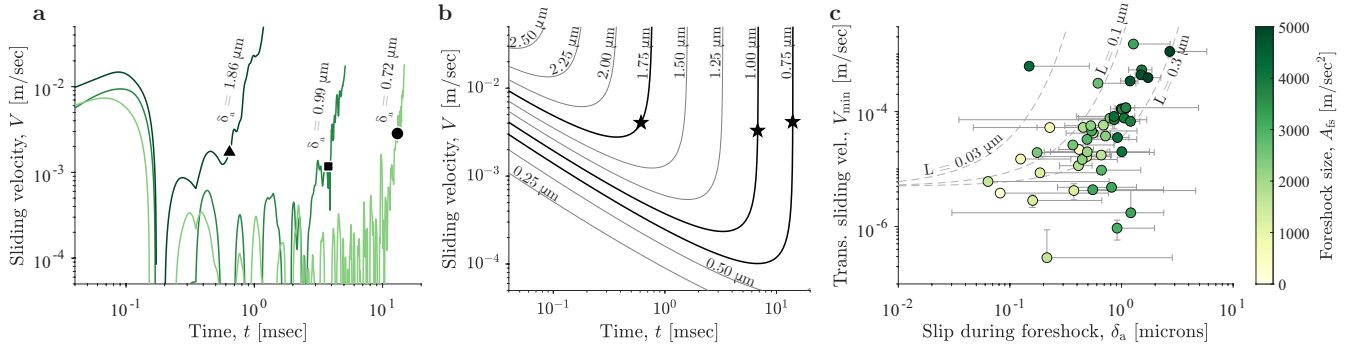


**Figure 3. Foreshock size predicts the transient sliding velocity of the nucleating patch.** **a**, The evolution of sliding velocity in time for the three events shown in Fig. 2. The moment where rupture velocity surpasses 10 m/sec is shown with a black symbol. Note the initial value of sliding velocity due to the foreshock, the reduction in sliding velocity after the foreshock, and the reacceleration of sliding velocity up to the dynamic rupture propagation. The foreshocks of these three events have estimated slips,  $\delta_a$ , of 0.72, 0.99, and 1.86 microns in order of increasing foreshock size,  $A_{fs}$  (see Methods). **b**, EoM simulation runs for various foreshock sizes, characterized by an asperity slip,  $\delta_a$ , given for each simulation. The simulations with  $\delta_a$  most closely corresponding to the experimental events in **a** are shown with dark lines and the moment they reach  $v_r = 10$  m/sec is indicated by a star (Fig. S10). The overstress is taken as  $\Delta f_0 = 0$ . **c**, The transient sliding velocity after the foreshock versus the slip accrued during the foreshock. After the foreshock, the slip evolves as an exponential function of time (Fig. S3). This evolution is fit and its derivative is evaluated just after the foreshock, yielding the initial minimum sliding velocity of the patch at the onset of nucleation. The slip accrued during the foreshock;  $\delta_a$ , is taken as the jump in slip at the moment of the foreshock (Fig. S3). Larger foreshocks yield larger transient sliding velocities. This result is predicted by the EoM, considering  $\frac{a}{b} = 0.55$ , state-evolution slip distances,  $L = 0.03, 0.1, 0.3$  microns, and ambient fault sliding velocity,  $V_0 = 10^{-6}$  m/sec. The dashed lines represent EoM predictions for the case with non-negative overstress. Events with negative overstress are predicted to fall below these lines and are characterized by lower  $V_{min}$  and longer nucleation duration. For **a** and **c**, the foreshock amplitude is given by the color bar. The error of  $\delta_a$  is estimated as the difference between the recorded value and the maximum possible value of  $\delta_a$  within 0.5 msec of the end of the foreshock. The error of  $V_{min}$  is estimated by propagating the error of the 95% confidence interval of the exponential fit to the slip versus time data.

to a quasi-static slip phase, before both sliding velocity and rupture velocity accelerate exponentially (Fig. S3), ultimately leading to dynamic rupture onset.

While natural earthquake rupture may not always be triggered by discrete foreshocks, larger foreshocks lead to higher transient sliding velocities  $V_{min}$ , both during and immediately following such precursory activity. This trend is clearly evident in our experimental data, where larger foreshocks correlate with higher values of  $V_{min}$  (Fig. 3c).

## Equation of motion

We now seek to reconcile our experimental observations with a state-of-the-art rupture model, grounded in rate-and-state friction. Garagash<sup>9</sup> developed an equation of motion (EoM) linking rate-and-state parameters and loading conditions to describe the nucleation and propagation of frictional ruptures. It reads:

$$K_{bg}(\Delta f_0; \ell, v_r) + K_{fs}(\Delta T; \ell) = K_c(v_r). \quad (1)$$

Here, all terms are implicit functions of the frictional parameters  $(a, b, L)$ , where  $a$ ,  $b$ , and  $L$  are the direct effect, evolution effect, and state-evolution slip distance, respectively.  $K_{bg}$  is the stress intensity factor (SIF) due to the background stress. It depends on the initial overstress  $\Delta f_0$  at ambient sliding velocity  $V_0$ , the crack length  $\ell$  and rupture velocity  $v_r$ , following rate-and-state friction.  $K_{fs}$  denotes the SIF contribution from the foreshock and depends on  $\ell$  and a localized Coulomb force of magnitude  $\Delta T \propto \mu' \delta_a$ , where  $\mu'$  is the apparent shear modulus and  $\delta_a$  the asperity slip. Ultimately, the two SIF contributions must balance the fault toughness  $K_c$ , which increases with  $v_r$ , owing to the rate-dependent frictional response. The exact form of the SIFs is not required to qualitatively match experimental observations, as long as  $K_{bg}$  increases with  $\ell$ , but  $K_{fs}$  decreases with  $\ell$ . This defines a ‘well’ in the energy available to drive the rupture at some intermediate crack length<sup>20,21</sup>, which when balanced with  $K_c(v_r)$ , sets a transient minimum in the rupture propagation and sliding velocities (Methods).

Nucleation dynamics are therefore controlled by two parameters,  $\Delta f_0$  and  $\Delta T$ , which scale the aforementioned dependence of  $K_{bg}$  and  $K_{fs}$  on the crack length, respectively. As shown in Fig. S9, the EoM predicts three possible nucleation scenarios: (i)



a transient deceleration followed by arrest without the nucleation of dynamic rupture; (ii) deceleration to  $V_{\min}$  followed by a prolonged quasi-static phase during which both slip and rupture velocity accelerate, eventually transitioning to the dynamic rupture; or (iii) near-immediate acceleration into dynamic rupture, without a quasi-static phase. All three behaviors are observed in our experimental dataset (Fig. S8, Fig. 3a, Fig. S7), and can be rationalized using the EoM. Indeed, following Equation (1), rupture initiation is initially driven by the impulsive force  $\Delta T$ . As the crack grows, the foreshock contribution  $K_{fs}$  decreases with increasing  $\ell$ , promoting rupture deceleration. However, the background contribution  $K_{bg}$  increases with  $\ell$  and tends to accelerate the crack. Crack growth, in turn, raises the sliding velocity  $V$ , which increases the transient stress drop, owing to the rate-weakening nature of the interface, and feeds  $K_{bg}$ . This feedback can sustain or arrest rupture depending on foreshock magnitude, represented by  $\Delta T$ , as it defines early-stage sliding velocity and thus the transient strength of the interface. When  $\Delta T$  is too small, the increase in  $K_{bg}$  with increasing crack length  $\ell$  is insufficient to offset the associated decrease in  $K_{fs}$ , and rupture arrests (Regime 1). In contrast, a large  $\Delta T$  generates high transient sliding velocities, leading to rapid growth of  $K_{bg}$  and immediate transition to dynamic rupture (Regime 3). Between these extreme cases, a moderate  $\Delta T$  induces a slower but self-sustained increase in  $K_{bg}$ , reinforced by the positive feedback of  $\ell$  and  $V$ , resulting in delayed dynamic rupture (Regime 2). Here, the overstress  $\Delta f_0$  primarily sets the baseline value of the transient stress drop and thus controls the threshold values of  $\Delta T$  that determine the transition between nucleation regimes.

Moreover, the EoM offers an explanation for the observed variability of the nucleation length  $\ell_c$  and the lack of a clear correlation with normal stress  $\sigma$  (Fig. 4b), which is otherwise expected in nucleation models<sup>5,6,22</sup> and reported in some experimental studies<sup>11,23,24</sup>, neither of which generally consider impulses. The EoM's predicted nucleation size for aging frictional faults is bounded by the maximum value  $\ell_{\infty} \approx \frac{1}{\pi} \frac{1}{(1-a/b)^2} \frac{\mu' L}{b \sigma}$ . This terminal value is however approached by nucleation transients driven by a vanishingly small impulse on a neutrally or slightly understressed faults (Fig. S2). Otherwise, both the overstress and the impulse imparted by the foreshock act to materially reduce the nucleation length compared to  $\ell_{\infty}$  by as much as an order of magnitude (Fig. S2).

In summary, the EoM offers a physical explanation for observed rupture behavior during nucleation. The advancing crack tip draws energy both from the foreshock and from the inherent stress state along the fault. However, these two contributions are not necessarily readily constrainable in both laboratory and natural settings. Instead, as these two components are the only contributors to the energy balance of the EoM, their combination results in one unique nucleation behavior or crack development path (Fig. 3b). In Regimes 1 and 2, this unique crack development path is characterized by the minimum transient sliding velocity  $V_{\min}$  which then, as a single parameter, dictates nucleation behavior (Fig. S5a).

## Transient sliding velocity controls earthquake nucleation

The nucleation length of the experimental events is positively correlated with the nucleation duration (Fig. 4b). This trend holds not only in our experiments, but also in larger-scale ( $\sim 1$  m) rock friction experiments and for quasi-statically slipping patches of natural earthquakes, where the onset of nucleation is identified by a foreshock. These foreshocks provide an empirical basis for estimating nucleation duration,  $\Delta t_c$ . Larger impulsive forces (i.e., larger foreshocks) result in higher transient minimum sliding velocities  $V_{\min}$  (Fig. 3b,c) and shorter nucleation duration  $\Delta t_c$ . At “large” sliding velocities  $V_{\min}$ ,  $\Delta t_c$  scales as the inverse of  $V_{\min}$ ,  $\Delta t_c \propto \frac{L}{V_{\min}}$ . However, a progressive shift from this inverse power-law behavior to a constant nucleation duration  $\Delta t_c \simeq \Delta t_0$  is predicted at the transition between Regimes 1 and 2, when  $V_{\min}$  approaches the ambient sliding velocity  $V_0$  (Fig. S5c). The relationship between  $\Delta t_c$  and  $V_{\min}$  is quantitatively predicted by the EoM using the frictional properties of PMMA and realistic laboratory values for the state evolution slip distance  $L$ , Equation (17).

Remarkably, the observed dependence of nucleation duration on transient sliding velocity appears to extend to quasi-static slip patches preceding certain natural earthquakes (Fig. 4d). The slope of this relationship is consistent between our laboratory experiments and natural events, but the natural earthquake data are offset by several orders of magnitude. This offset implies that, for a given transient velocity, natural faults exhibit significantly longer nucleation durations than those observed in the laboratory. This shift is attributable to differences in frictional properties, specifically much larger state evolution slip distances and smaller values of the rate-weakening coefficient  $b - a$  for natural faults, which may depend on fault lithology<sup>37</sup>. Additionally, part of the discrepancy may stem from the uncertainty in estimating transient sliding velocities for natural earthquakes; our values, based on indirect constraints, likely overestimate the  $V_{\min}$  during nucleation. Nevertheless, variations in the  $a/b$  ratio arising from possible differences in rheology and/or variations of state-evolution slip distance  $L$ , possibly related to fault maturity<sup>38</sup>, are sufficient to explain the discrepancies observed among the different earthquakes analyzed (Fig. 4d).

Our experimental results provide new insight into the physics of earthquake nucleation and allow us to revisit several key questions regarding the onset of seismic rupture. (i) *Are all earthquakes preceded by a nucleation phase?* In our laboratory experiments, all dynamic events exhibiting measurable nucleation phases are initiated by foreshocks, which give rise to transient sliding and quasi-static slip prior to dynamic rupture. However, we also observe events in which the foreshock directly transitions into dynamic rupture without a discernible (quasi-static) nucleation phase. This suggests that while a nucleation

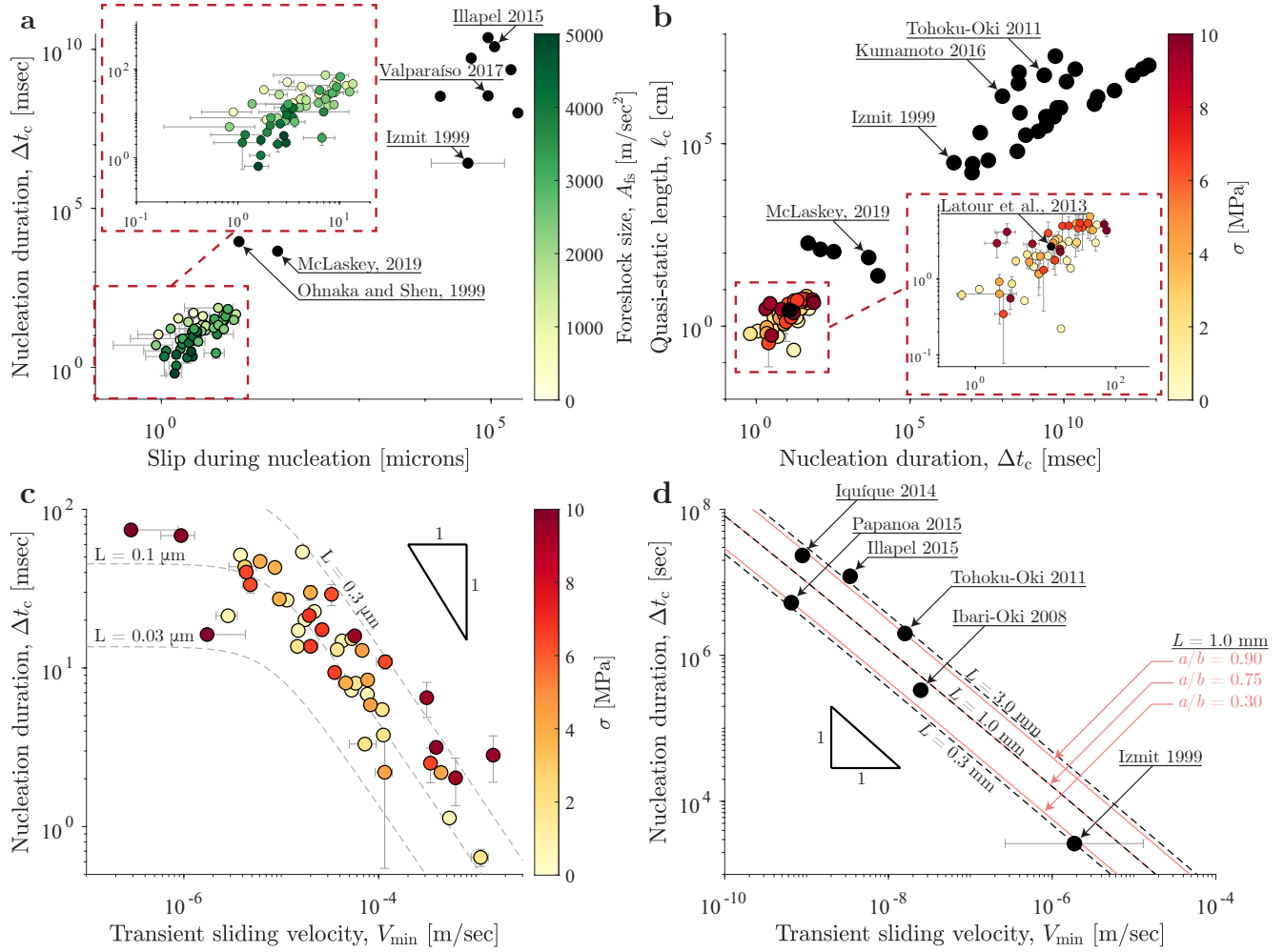


**Figure 4. Transient sliding velocity predicts nucleation duration and length.** **a**, The correlation between the nucleation duration and the slip accrued during nucleation. Prolonged nucleation phases are able to accrue more slip. Laboratory<sup>25,26</sup> and natural<sup>12,14,15,18,27–31</sup> earthquakes are included with black dots. The foreshock amplitude is given by the color bar. **b**, The nucleation length,  $\ell_c$ , as a function of the nucleation duration,  $\Delta t_c$ . The error of both  $\ell_c$  and  $\Delta t_c$  was found by reassessing both quantities with a rupture velocity of 20 m/sec. Natural<sup>12,14,15,18,27–34</sup> and laboratory<sup>11,25,26,35,36</sup> earthquakes are plotted with black dots. **c**, The nucleation duration as a function of the transient sliding velocity after the foreshock. Predictions from the EoM are shown in grey dashed lines based on state-evolution aging law slip distances,  $L$ , of 0.03, 0.1, and 0.3 microns,  $a/b = 0.55$ , and an ambient sliding velocity of  $10^{-6}$  m/sec. For **b** and **c**, the local value of normal stress is given by the color bar, demonstrating an apparent independence of all three parameters on normal stress. **d**, The duration and transient sliding velocity of the nucleation phases of natural earthquakes<sup>12,14,18,28–31</sup>. Note that the number of points is limited due to the scarcity of resolved instances of fault slip during a foreshock to main shock sequence, required here for the analysis. EoM fits are provided for state-evolution aging law slip distances of 0.3, 1.0, and 3.0 mm using  $a/b = 0.75$  and an ambient sliding velocity of  $10^{-12}$  m/sec and shown in dashed lines. Additionally, fits with  $L = 1.0$  mm and  $a/b = 0.30, 0.75, 0.90$  are shown in pink. Assuming different values for the natural fault ambient sliding velocity, as long as it remains much smaller than the transient  $V_{min}$ , does not materially affect the EoM fits. The error in  $\ell_c$  and  $\Delta t_c$  are estimated considering dynamic rupture beginning at 20 m/sec instead of 10 m/sec. The error for the slip during nucleation is estimated by evaluating the slip within 0.1 msec of  $v_r$  reaching 10 m/sec.

phase often occurs, it is not a strict prerequisite for rupture. (ii) *How does the occurrence of a foreshock influence the nucleation of a large earthquake?* On rate-weakening faults, foreshocks initiate a positive feedback loop between the sliding velocity and the stress drop, causing  $K_{bg}$  to eventually grow to the dynamic range of the rate-dependent fault toughness  $K_c(v_r)$  with  $v_r \sim c_s$ . This drives the growth of the aseismically-slipping patch and causes main shock nucleation in sufficiently-stressed conditions, making rate-weakening interfaces foreshock sensitive, especially when compared to rate-independent frameworks, and providing a mechanism compatible with cascade-like processes. Larger foreshocks shrink the time scale and reduce the stress criticality required for nucleation. The largest foreshocks can themselves merge into a main shock. Yet, observations of quasi-static nucleation phases in foreshock to main shock sequences are relatively rare in nature, likely because the impulses of most foreshocks are either too insignificant to lead to nucleation after the initial slowdown (Regime 1), too large to not directly merge into a main shock (Regime 3), or quasi-static phases are simply too difficult to identify in observations<sup>17</sup>. Importantly, nucleation can begin without an identifiable foreshock. In this case, rupture is either initiated directly (Regime 3) or through a quasi-static nucleation phase without a foreshock, in which the impulse is supplied by tectonic loading or other aseismic processes<sup>6</sup>. (iii) *Does the characteristic slip distance representative of dynamic rupture also describe nucleation?* These results allow for the inference of reasonable ranges (between 0.3 and 3 mm) of state-evolution slip distances,  $L$ , of real earthquakes during their nucleation phases (Fig. 4d). These are a notable departure from the larger values of  $L$  inferred for dynamic rupture; e.g., the state-evolution distance of 0.8 m used for modeling Tohoku-Oki<sup>39</sup>.

Taken together, our results demonstrate that nucleation is a dynamic, rate-dependent process that can manifest in multiple forms, and whose characteristics hold important implications for understanding the conditions under which rupture initiates and evolves. Beyond earthquakes, our results highlight a fundamental mechanism of frictional failure that may also govern the stability of engineered and tribological interfaces as well as landslides and icequakes.

## Acknowledgments

B.F. and F.P. acknowledge funding from the European Union (ERC Starting Grant HOPE num. 101041966). Corentin Noël, Federica Paglialunga, and Julien Ambre are thanked for their help in preparing the sample and setup. Xin Cui, Jean-Paul Ampuero and Frédéric Cappa are thanked for helpful discussions.

## Data availability

Data are available at doi:10.5281/zenodo.17185894.

## Code availability

The code will be available in the online repository at doi:10.5281/zenodo.17185894 upon acceptance of the manuscript. All information and details necessary to reproduce the theoretical development are described in the Methods.

## Inclusion & Ethics

This study did not involve human participants, animal subjects, or fieldwork requiring community engagement. Therefore, issues relating to inclusion, diversity, or ethics in participant recruitment and representation do not apply. All experimental procedures were conducted in accordance with standard laboratory safety and ethical research practices.

## References

- Ohnaka, M. A constitutive scaling law and a unified comprehension for frictional slip failure, shear fracture of intact rock, and earthquake rupture. *J. Geophys. Res.* **108** (2003). <https://doi.org/10.1029/2000JB000123>.
- Ida, Y. Cohesive force across the tip of a longitudinal-shear crack and Griffith's specific surface energy. *J. Geophys. Res.* **77** (1972). <https://doi.org/10.1029/JB077i020p03796>.
- Dieterich, J. Modeling of rock friction 1. Experimental results and constitutive equations. *J. Geophys. Res.* **84**, 2161–2168 (1979). <https://doi.org/10.1029/JB084iB05p02161>.
- Campillo, M. & Ionescu, I. Initiation of antiplane shear instability under slip dependent friction. *J. Geophys. Res.* **102**, 20363–20371 (1997). <https://doi.org/10.1029/97JB01508>.
- Uenishi, K. & Rice, J. Universal nucleation length for slip-weakening rupture instability under nonuniform fault loading. *J. Geophys. Res.* **108** (2003). <https://dx.doi.org/10.1029/2001JB001681>.
- Rubin, A. & Ampuero, J. Earthquake nucleation on (aging) rate and state faults. *J. Geophys. Res.* **110** (2005). <https://doi.org/10.1029/2005JB003686>.



- 183 7. Gvirtzman, S., Kammer, D., Adda-Bedia, M. & Fineberg, J. How frictional ruptures and earthquakes nucleate and evolve.  
184 *Nature* **637**, 369–374 (2025). <https://doi.org/10.1038/s41586-024-08287-y>.
- 185 8. Dieterich, J. A model for the nucleation of earthquake slip. In Das, S., Boatwright, J. & Scholz, C. (eds.) *Geophysical*  
186 *Monograph Series* (1986).
- 187 9. Garagash, D. Fracture mechanics of rate-and-state faults and fluid injection induced slip. *Philos. Transactions Royal Soc.*  
188 *A* **379** (2021). <https://doi.org/10.1098/rsta.2020.0129>.
- 189 10. Lebihain, M., Roch, T., Violay, M. & Molinari, J. Earthquake nucleation along faults with heterogeneous weakening rate.  
190 *Geophys. Res. Lett.* **48** (2021). <https://doi.org/10.1029/2021GL094901>.
- 191 11. Latour, S., Schubnel, A., Nielsen, S., Madariaga, R. & Vinciguerra, S. Characterization of nucleation during laboratory  
192 earthquakes. *Geophys. Res. Lett.* **40**, 5064–5069 (2013). <https://doi.org/10.1002/grl.50974>.
- 193 12. Kato, A. *et al.* Propagation of slow slip leading up to the 2011  $M_w$  9.1 Tohoku-Oki Earthquake. *Science* **335**, 705–708  
194 (2012). <https://doi.org/10.1126/science.1215141>.
- 195 13. Ruiz, S. *et al.* Intense foreshocks and a slow slip event preceded the 2014 Iquique  $M_w$  8.4 earthquake. *Science* **345**,  
196 1165–1169 (2014). <https://doi.org/10.1126/science.125607>.
- 197 14. Kato, A., Fukuda, J., Kumazawa, T. & Nakagawa, S. Accelerated nucleation of the 2014 Iquique, Chile  $M_w$  8.2 earthquake.  
198 *Sci. Reports* **6** (2016). <https://doi.org/10.1038/srep24792>.
- 199 15. Ruiz, S. *et al.* Nucleation phase and dynamic inversion of the  $M_w$  6.9 Valparaíso 2017 earthquake in central Chile.  
200 *Geophys. Res. Lett.* **44**, 10290–10297 (2017). <https://doi.org/10.1002/2017GL075675>.
- 201 16. Socquet, A. *et al.* An 8 month slow slip event triggers progressive nucleation of the 2014 Chile megathrust. *Geophys. Res.*  
202 *Lett.* **44**, 4046–4053 (2017). <https://doi.org/10.1002/2017GL073023>.
- 203 17. Blettery, Q. & Nocquet, J. The precursory phase of large earthquakes. *Science* **381**, 297–301 (2023).  
204 <https://doi.org/10.1126/science.adg256>.
- 205 18. Bouchon, M. *et al.* Extended nucleation of the 1999  $M_w$  7.6 Izmit Earthquake. *Science* **331**, 877–880 (2011).  
206 <https://doi.org/10.1126/science.1197341>.
- 207 19. Bouchon, M., Durand, V., Marsan, D., Karabulut, H. & Schmittbuhl, J. The long precursory phase of most large interplate  
208 earthquakes. *Nat. Geosci.* **6**, 299–302 (2013). <https://doi.org/10.1038/NGEO1770>.
- 209 20. Ripperger, J., Ampuero, J., Mai, P. & Giardini, D. Earthquake source characteristics from dynamic rupture with constrained  
210 stochastic fault stress. *J. Geophys. Res.* **112** (2007). <https://dx.doi.org/10.1029/2006JB004515>.
- 211 21. Garagash, D. & Germanovich, L. Nucleation and arrest of dynamic slip on a pressurized fault. *J. Geophys. Res.* **117**, DOI:  
212 <https://doi.org/10.1029/2012JB009209> (2012).
- 213 22. Rice, J. & Ruina, A. Stability of steady frictional slipping. *J. Appl. Mech.* **50**, 343–349 (1983).  
214 <https://doi.org/10.1115/1.3167042>.
- 215 23. Ji, Y., Wang, L., Hofmann, H., Kwiatak, G. & Dresen, G. High-rate fluid injection reduces the nucleation of laboratory  
216 earthquakes on critically stressed faults in granite. *Geophys. Res. Lett.* **49** (2022). <https://doi.org/10.1029/2022GL100418>.
- 217 24. Marty, S. *et al.* Nucleation of laboratory earthquakes: Quantitative analysis and scalings. *J. Geophys. Res. Solid Earth* **128**  
218 (2023). <https://doi.org/10.1029/2022JB026294>.
- 219 25. Ohnaka, M. & Shen, L. Scaling of the shear rupture process from nucleation to dynamic propagation: Implications of  
220 geometric irregularity of the rupturing surfaces. *J. Geophys. Res.* **104**, 817–844 (1999).
- 221 26. McLaskey, G. Earthquake initiation from laboratory observations and implications for foreshocks. *J. Geophys. Res. Solid*  
222 *Earth* **124**, 12882–12904 (2019). <https://doi.org/10.1029/2019JB018363>.
- 223 27. Kato, A., Fukuda, J., Nakagawa, S. & Obara, K. Foreshock migration preceding the 2016  $M_w$  7.0 Kumamoto earthquake,  
224 Japan. *Geophys. Res. Lett.* **43**, 8945–8953 (2016). <https://doi.org/10.1002/2016GL070079>.
- 225 28. Radiguet, M. *et al.* Triggering of the 2014  $M_w$  7.3 Papanoa earthquake by a slow slip event in Guerrero, Mexico. *Nat.*  
226 *Geosci.* **9**, 829–833 (2016). <https://doi.org/10.1038/NGEO2817>.
- 227 29. Ellsworth, W. & Bulut, F. Nucleation of the 1999 Izmit earthquake by a triggered cascade of foreshocks. *Nat. Geosci.* **11**,  
228 531–535 (2018). <https://doi.org/10.1038/s41561-018-0145-1>.
- 229 30. Nishikawa, T. & Ide, S. Recurring slow slip events and earthquake nucleation in the source region of the M 7 Ibaraki-Oki  
230 earthquakes revealed by earthquake swarm and foreshock activity. *J. Geophys. Res. Solid Earth* **123**, 7950–7968 (2018).  
231 <https://doi.org/10.1029/2018JB015642>.

31. Huang, H. & Meng, L. Slow unlocking processes preceding the 2015 Mw 8.4 Illapel, Chile, earthquake. *Geophys. Res. Lett.* **45**, 3914–3922 (2018). <https://doi.org/10.1029/2018GL077060>.
32. Whitcomb, J., Garmany, J. & Anderson, D. Earthquake prediction: Variation of seismic velocities before the San Francisco Earthquake. *Science* **180**, 632–635 (1973). [10.1126/science.180.4086.632](https://doi.org/10.1126/science.180.4086.632).
33. Eyre, T. *et al.* The role of aseismic slip in hydraulic fracturing-induced seismicity. *Sci. Adv.* **5** (2019). <https://doi.org/10.1126/sciadv.aav7172>.
34. Karabulut, H., Güvercin, S., Eskiköy, F., Konca, A. & Ergintav, S. The moderate size 2019 September  $M_w$  5.8 Silivri earthquake unveils the complexity of the Main Marmara Fault shear zone. *Geophys. J. Int.* **224**, 377–388 (2020). <https://doi.org/10.1093/gji/ggaa469>.
35. Yamashita, F. *et al.* Two end-member earthquake preparations illuminated by foreshock activity on a meter-scale laboratory fault. *Nat. Commun.* **12** (2021). <https://doi.org/10.1038/s41467-021-24625-4>.
36. Xu, S. *et al.* Fault strength and rupture process controlled by fault surface topography. *Nat. Geosci.* **16**, 94–100 (2023). <https://doi.org/10.1038/s41561-022-01093-z>.
37. Blanpied, M., Lockner, D. & Byerlee, J. Fault stability inferred from granite sliding experiments at hydrothermal conditions. *Geophys. Res. Lett.* **18**, 609–612 (1991). <https://doi.org/10.1029/91GL00469>.
38. Gabriel, A.-A., Garagash, D. I., Palgunadi, K. H. & Mai, P. M. Fault size–dependent fracture energy explains multiscale seismicity and cascading earthquakes. *Science* **385**, eadj9587 (2024).
39. Kozdon, J. & Dunham, E. Rupture to the trench: Dynamic rupture simulations of the 11 March 2011 Tohoku Earthquake. *Bull. Seismol. Soc. Am.* **103**, 1275–1289 (2013). <https://doi.org/10.1785/0120120136>.
40. Rosakis, A., Samudrala, O. & Coker, D. Cracks faster than the shear wave speed. *Science* **284**, 1337–1340 (1999). <https://doi.org/10.1126/science.284.5418.1337>.
41. Nielsen, S., Taddeucci, J. & Vinciguerra, S. Experimental observation of stick-slip instability fronts. *Geophys. J. Int.* **180**, 697–702 (2010). <https://doi.org/10.1111/j.1365-246X.2009.04444.x>.
42. Schubnel, A., Nielsen, S., Taddeucci, J., Vinciguerra, S. & Rao, S. Photo-acoustic study of subshear and supershear ruptures in the laboratory. *Earth Planet. Sci. Lett.* **308**, 424–432 (2011). <https://dx.doi.org/10.1016/j.epsl.2011.06.013>.
43. Nadeau, R. & Johnson, L. Seismological studies at Parkfield VI: Moment release rates and estimates of source parameters for small repeating earthquakes. *Bull. Seismol. Soc. Am.* **88**, 790–814 (1998). <https://doi.org/10.1785/BSSA0880030790>.
44. Zang, A. *et al.* Source analysis of acoustic emissions in Aue granite cores under symmetric and asymmetric compressive loads. *Geophys. J. Int.* **135**, 1113–1130 (1998). <https://doi.org/10.1046/j.1365-246X.1998.00706.x>.
45. Freund, L. *Dynamic Fracture Mechanics* (Cambridge University Press, 1990).
46. Cattania, C. A source model for earthquakes near the nucleation dimension. *Bull. Seismol. Soc. Am.* **113**, 909–923 (2023). <https://doi.org/10.1785/0120220045>.
47. Ruina, A. Slip instability and state variable friction laws. *J. Geophys. Res.* **88**, 10359–10370 (1983). <https://doi.org/10.1029/JB088iB12p10359>.
48. Ampuero, J. & Rubin, A. Earthquake nucleation on rate and state faults: Aging and slip laws. *J. Geophys. Res.* **113** (2008). <https://dx.doi.org/10.1029/2007JB005082>.
49. Baumberger, T., Berthoud, P. & Caroli, C. Physical analysis of the state- and rate-dependent friction law. II. Dynamic friction. *Phys. Rev. B* **60**, 3928–3939 (1999). <https://doi.org/10.1103/PhysRevB.60.3928>.
50. Viesca, R. Self-similar slip instability on interfaces with rate- and state-dependent friction. *Proc. Royal Soc. A: Math. Phys. Eng. Sci.* **472** (2016). <https://doi.org/10.1098/rspa.2016.0254>.

## Supplementary Files

This is a list of supplementary files associated with this preprint. Click to download.

- [Methods.pdf](#)